Dynamical solutions for migration of chiral DNA-type objects in shear flows

Peilong Chen and Qiyi Zhang

Department of Physics and Center for Complex Systems, National Central University, Chungli 320, Taiwan

We present a dynamical analysis of chiral object motions to explain physical mechanisms and give quantitative predictions on the shear-induced drift motions of chiral objects and the chiral separation of enantiomers using shear flows. For objects well represented by the uniaxial approximation, such as DNA and chiral disk hexamers, dynamical motions in low-Reynolds-number shear flows are solved analytically, in terms of steady-state object-flow interacting parameters, which can be calculated numerically by well-established methods. The shear-induced drifting speed of long helices are evaluated. Good agreements are found between our results and those obtained from dynamical simulations [Makino and Doi, Phys. Fluids **17**, 103605 (2005)]. We also compare our results with those obtained experimentally [Marcos, Fu, Powers, and Stocker, Phys. Rev. Lett. **102**, 158103 (2009)]. The analysis may also be extended to study other important chiral-flow interactions in nature environments and microfluidic devices, such as the particle-wall and interparticle interactions.

PACS number(s): 47.15.G−, 81.05.Xj, 46.70.Hg

I. INTRODUCTION

With increasing interests on the interplay between fluid flows and microscopic-scale objects (e.g., bacteria and macromolecules) and widespread usage of microfluidic devices, understanding complex motions of chiral objects in shear flows becomes a very important issue [1–5]. Chiral biological macromolecules (e.g., DNA) are mostly in the liquid environment and their artificial controls/manipulations are almost always in fluids, signifying the importance of chiral-flow interaction. Chirality is also abundant at larger scales, for example the swimming of *E. coli* through rotations of helical flagella [6]. There are also possible thermomechanical couplings for chiral particles [7].

One actively pursued topic is the use of shear flows to separate chiral objects and their mirror-reflected but distinct counterparts (enantiomers) [4,5,8]. This method could improve on the currently established ones of using specific chiral crystal channels which are often molecular specific and have low efficiency [9]. Experimentally shear-induced drifting was indeed demonstrated using helical-shaped bacteria in a microfluidic flow cell [5], and forces for fixed screws in shear flows were also directly measured [8].

However, theoretical advance is hampered by the lack of concrete analytical results. We mostly have direct dynamical numerical simulations of the low-Reynolds-number (Stokes) flow equations of motion, such as the simulations of twisted ribbonlike particles under shear [4]. However, besides numerical data, simulations provide few insights into the underlining physical mechanisms. On the other hand, chirality is always somewhat puzzling and there are strong interests in better theoretical understanding of the degree of chirality [10–12], a difficult goal for numerical calculations. It is indeed recognized that there are no universal chiral order parameters, and different physical properties will depend on different ones.

In this paper we consider chiral objects under shear and solve for their rigid body motion. We are most interested in the rotational dynamics and the average drifting motion in the vorticity direction. The drifting has been previously recognized [4] from simple symmetry arguments to depend on one single chiral parameter for uniaxial chiral objects,

although the chiral parameter can only be calculated with direct dynamical simulations. Our analysis derives how the chiral parameter depends on various steady-state object-flow interacting parameters. Thus the mechanism of chiral separation by shear flow can be fully understood and quantitative predictions are provided. The key to the analysis is the separation of the flow field into two components to fully utilize the symmetries of the uniaxial chiral objects and shear flows. Comparisons with simulation and experimental results are also presented. Further modification and extension of our analysis could likely be used to study other important chiral-flow interactions, such as how the chiral objects could interact with a fixed wall or with each other dynamically.

Consideration of uniaxial chiral objects actually is not as restrictive as it seems. Similar to nematic liquid crystals, straight helices such as DNA should be well approximated, due mainly to the expected fast rotations around the central axis. Chiral disk objects are also good candidates, with examples like the chiral benzene-centered, phthalocyanine hexamers [13], which basically look like six-bladed propellers, and curious molecular Möbius strips [14]. There are also near spherical-shaped chiral molecules [15].

II. EQUATIONS OF MOTION AND SYMMETRIES

Consider a rigid body which is moving in a viscous fluid with a velocity $\boldsymbol{v}$ and rotation $\boldsymbol{\omega}$ under an external shear. In the limit of a low Reynolds number the fluids follow the Stokes flow equation of motion:

$$\nabla P = \eta \nabla^2 \boldsymbol{u}, \tag{1}$$

with P being the pressure, η being the viscosity, and $\boldsymbol{u}$ being the flow velocity which follows the no-slip boundary condition on the object surface.

Because Eq. (1) is linear, we can consider the flow field under shear to consist of two parts, both of which follow Eq. (1) but have different boundary conditions. The first part, $\boldsymbol{u}_a(\boldsymbol{r})$, matches the velocity on the surface of the rigid object, and $\boldsymbol{u}_a(\boldsymbol{r} \to \infty) = 0$. The second, $\boldsymbol{u}_b(\boldsymbol{r})$, is zero on the object surface and matches the simple shear flow at infinity. The sum

$u_a(r) + u_b(r)$ matches both the no-slip boundary conditions at the moving object surface and the external simple shear. Then v and ω are determined by the conditions of zero total force and torque on the object, due to the negligible momentum in the Stokes flow dynamics. The advantage of separating the flow field into two parts is that the shear-induced $u_b(r)$ is analyzed with the object fixed in both position and orientation. Additional symmetries of the object then make the calculation of the force f_b and torque τ_b due to u_b much easier.

The force f_a and torque τ_a due to u_a are just the resistance force and torque as the object moves in an otherwise stationary fluid. Because the Stokes flow is linear, f_a and τ_a are in the linear matrix form:

$$f_a = a \cdot v + b \cdot \omega,$$
$$\tau_a = b \cdot v + c \cdot \omega.$$

Here a, b, and c are the second-rank resistance tensors depending on the object shape. The cross terms, b, are the same due to the Lorentz reciprocal theorem [16]. On the other hand, f_b and τ_b couple to the second-rank velocity gradient tensor $e = \nabla u_s$ (with u_s being the applied simple shear flow) through third-rank tensors: $f_b = g : e$ and $\tau_b = h : e$. The tensors g and h are determined by the object shape and follow tensor rotating rules when the object rotates in space. Any symmetry of the object shape will reflect on g and h. Now the force and torque free requirements,

$$f_a + f_b = a \cdot v + b \cdot \omega + g : e = 0, \tag{2}$$
$$\tau_a + \tau_b = b \cdot v + c \cdot \omega + h : e = 0, \tag{3}$$

provide the equations to determine the velocity v and rotation ω.

Generally, if $(\hat{m}_1, \hat{m}_2, \hat{m}_3)$ is a set of orthogonal unit vectors inscribed in the object, the third-rank tensors g and h can be expressed as

$$g = \psi_{ijk} \hat{m}_i \hat{m}_j \hat{m}_k, \tag{4}$$
$$h = \phi_{ijk} \hat{m}_i \hat{m}_j \hat{m}_k. \tag{5}$$

The Einstein notation of summing one to three over repeated indices is used and, hereafter, we define $(g : e)_k = g_{ijk} e_{ji}$. The parameters ψ_{ijk} and ϕ_{ijk} characterize the object-shear flow interaction.

Symmetry of the object could simplify g and h. Specifically, if $\hat{m}_1$ is a two-fold symmetry axis, a π rotation about the $\hat{m}_1$ axis leaves the object (hence g and h) unchanged. Nevertheless both $\hat{m}_2$ and $\hat{m}_3$ change signs under such a rotation. So total numbers of $\hat{m}_2$ and $\hat{m}_3$ in each term of Eqs. (4) and (5) need to be even, thus excluding the terms $\hat{m}_2 \hat{m}_2 \hat{m}_2$ and $\hat{m}_3 \hat{m}_3 \hat{m}_3$. Also $\hat{m}_1$ can only appear an odd number of times in each term. Accordingly, if the object possesses at least two two-fold symmetry axes and two of the $\hat{m}_i$ are chosen in these axes, then each of g and h only has six terms:

$$g = \psi_{ijk} \hat{m}_i \hat{m}_j \hat{m}_k, \quad i \neq j \neq k \neq i. \tag{6}$$
$$h = \phi_{ijk} \hat{m}_i \hat{m}_j \hat{m}_k,$$

Thus the object will experience force and torque only in the vorticity direction under a simple shear flow when the velocity and velocity gradient of the shear are along two of the $\hat{m}_i$.
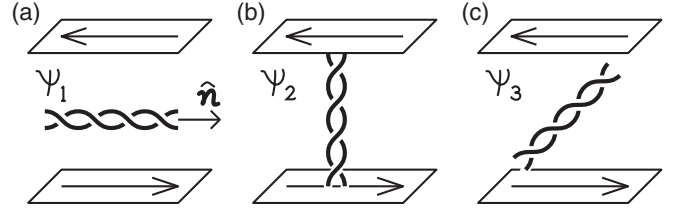
FIG. 1. Relation between orientation and ψ_i, with a double helix used as an example of a uniaxial object.

III. UNIAXIAL APPROXIMATION

Solving Eqs. (2) and (3) for a general shaped object exactly will be complicated. We thus consider uniaxial chiral objects which possess a rotational symmetry axis such that, besides being chiral, the object's orientation in the space is defined completely by a director $\hat{n}$ (with $\pm \hat{n}$ being equivalent).

Uniaxial objects have the nice properties that the resistance tensors a, b, and c are all in the form of, due to the rotational symmetry around $\hat{n}$,

$$a = -a_{\parallel} \hat{n}\hat{n} - a_{\perp}(I - \hat{n}\hat{n}),$$

with $I_{ij} = \delta_{ij}$. Here negative signs are adopted to stress the resistance force/torque characters. Requirements for Eq. (6) are also satisfied with three two-fold symmetry axes. Assuming $\hat{n} = \hat{m}_3$, there is additional symmetry between $\hat{m}_1$ and $\hat{m}_2$, leading to $\psi_{213} = -\psi_{123}$, $\psi_{132} = -\psi_{231}$, and $\psi_{213} = -\psi_{123}$ (similarly for ϕ_{ijk}). Thus there are only three parameters left for g and h each:

$$g_{ijk} = \psi_1 n_j n_l \epsilon_{ilk} + \psi_2 n_i n_l \epsilon_{ljk} + \psi_3 n_k n_l \epsilon_{ijl},$$
$$h_{ijk} = \phi_1 n_j n_l \epsilon_{ilk} + \phi_2 n_i n_l \epsilon_{ljk} + \phi_3 n_k n_l \epsilon_{ijl}.$$

As illustrated in Fig. 1, ψ_1, ψ_2, and ψ_3 correspond to the forces in the vorticity direction experienced by the object under shear when $\hat{n}$ is fixed aligning in the velocity, velocity-gradient, and vorticity directions, respectively. Equivalently we can also write $g : e$ (with $e = \nabla u_s$) in the vector form:

$$g : e = \psi_1 [\nabla(\hat{n} \cdot u_s)] \times \hat{n} + \psi_2 \hat{n} \times [(\hat{n} \cdot \nabla)u_s]$$
$$+ \psi_3 [\hat{n} \cdot (\nabla \times u_s)]\hat{n}$$

A similar formulation also applies between h and ϕ.

Further symmetry arguments lead to the conclusions that b and g depend on chirality such that they will change sign if chirality is reversed and are zero for a chiral object. On the other hand, a, c, and h do not change with the reverse of chirality. Figure 2 shows the particular example for $c_{\perp}$ which
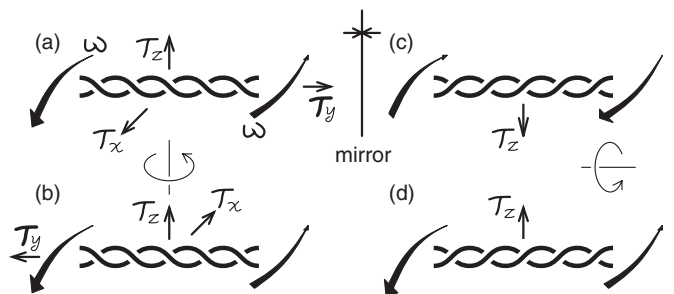
FIG. 2. Arguments leading to a nonchiral contribution to $c_{\perp}$.

couples the rotation $\omega \hat{z}$ with the torque (τ_x, τ_y, τ_z) experienced by the object (illustrated as a double helix). Now considering the π rotation around the z axis from (a) to (b), τ_z remains the same, but τ_x and τ_y change sign. However, since the rotation $\omega \hat{z}$ and the object remain the same, τ_x and τ_y are necessarily zero and only τ_z is possible. Next consider a mirror operation from (a) to (c) (note that τ_z changes direction in the mirror image), followed by a π rotation from (c) to (d). Comparing (a) and (d), the rotation and τ_z are the same, but the helix changes from a right-handed one to a left-handed one. Thus contribution to τ_z due to the rotation cannot depend on the chirality, as with $c_\perp$. All the other cases can be similarly demonstrated with suitable combinations of mirror and rotation operations.

Now, to solve for $\boldsymbol{v}$ and $\boldsymbol{\omega}$, we apply $\boldsymbol{a}^{-1}$ to Eq. (2) to get $\boldsymbol{v}$ and substitute $\boldsymbol{v}$ into Eq. (3) to obtain $\boldsymbol{\omega}$. With $\hat{\boldsymbol{n}}\hat{\boldsymbol{n}} \cdot \hat{\boldsymbol{n}}\hat{\boldsymbol{n}} = \hat{\boldsymbol{n}}\hat{\boldsymbol{n}}$, $\hat{\boldsymbol{n}}\hat{\boldsymbol{n}} \cdot (\boldsymbol{I} - \hat{\boldsymbol{n}}\hat{\boldsymbol{n}}) = 0$, and $(\boldsymbol{I} - \hat{\boldsymbol{n}}\hat{\boldsymbol{n}}) \cdot (\boldsymbol{I} - \hat{\boldsymbol{n}}\hat{\boldsymbol{n}}) = (\boldsymbol{I} - \hat{\boldsymbol{n}}\hat{\boldsymbol{n}})$, we quickly have

$$\boldsymbol{a}^{-1} = -\frac{1}{a_\parallel} \hat{\boldsymbol{n}}\hat{\boldsymbol{n}} - \frac{1}{a_\perp} (\boldsymbol{I} - \hat{\boldsymbol{n}}\hat{\boldsymbol{n}}).$$

Without the loss of generality, we choose the simple shear as $\boldsymbol{u}_s(\boldsymbol{r}) = -\dot{\gamma} y \hat{\boldsymbol{x}}$, with $\dot{\gamma}$ being the shear rate. After some straightforward algebra, we obtain the velocity $\boldsymbol{v}$ and rotation $\boldsymbol{\omega}$ of the object as

$$\boldsymbol{v} = \dot{\gamma}(\beta_1 n_1 \hat{\boldsymbol{n}} \times \hat{\boldsymbol{y}} + \beta_2 n_2 \hat{\boldsymbol{x}} \times \hat{\boldsymbol{n}} - \beta_3 n_3 \hat{\boldsymbol{n}}), \quad (7)$$

$$\boldsymbol{\omega} = \dot{\gamma}(\alpha_1 n_1 \hat{\boldsymbol{n}} \times \hat{\boldsymbol{y}} + \alpha_2 n_2 \hat{\boldsymbol{x}} \times \hat{\boldsymbol{n}} - \alpha_3 n_3 \hat{\boldsymbol{n}}) \quad (8)$$

with $\hat{\boldsymbol{n}} \equiv n_1 \hat{\boldsymbol{x}} + n_2 \hat{\boldsymbol{y}} + n_3 \hat{\boldsymbol{z}}$, and

$$\begin{aligned} \beta_i &\equiv (c_\perp \psi_i - b_\perp \phi_i)/q_\perp, \quad i = 1 \text{ or } 2, \\ \beta_3 &\equiv (c_\parallel \psi_3 - b_\parallel \phi_3)/q_\parallel, \\ \alpha_i &\equiv (a_\perp \phi_i - b_\perp \psi_i)/q_\perp, \quad i = 1 \text{ or } 2, \\ \alpha_3 &\equiv (a_\parallel \phi_3 - b_\parallel \psi_3)/q_\parallel. \end{aligned} \quad (9)$$

Here $q_\parallel \equiv a_\parallel c_\parallel - b_\parallel^2$ and $q_\perp \equiv a_\perp c_\perp - b_\perp^2$.

Furthermore $\boldsymbol{b}$ and $\boldsymbol{g}$ are not independent of each other. As illustrated in Fig. 3(a), since $b_\parallel$ is the force experienced along $\hat{\boldsymbol{n}}$ when the object rotates around $\hat{\boldsymbol{n}}$, it is also the force with the object fixed but the fluid counter-rotates. However, this counter-rotating fluid is exactly the sum of two simple shear flows, each of which could apply a force ψ_3 on the object. Thus we obtain $b_\parallel = 2\psi_3$. A similar argument in Fig. 3(b) leads to $b_\perp = \psi_1 + \psi_2$. The same considerations also lead to $c_\parallel = 2\phi_3$ and $c_\perp = \phi_1 + \phi_2$.
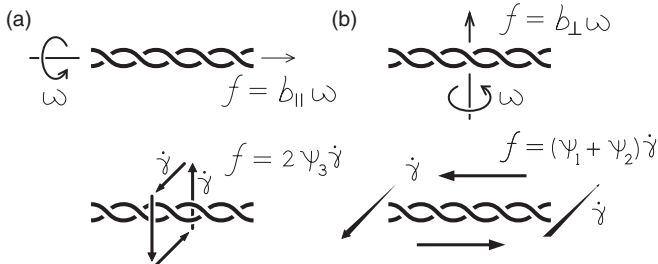
With these relationships, Eq. (9) is greatly simplified. Particularly, $\beta_3 = 0$ and

$$\beta_1 = -\beta_2 = (\phi_2 \psi_1 - \phi_1 \psi_2)/q_\perp \equiv \beta. \quad (10)$$

The dynamics is thus solved in terms of the parameters $a_\parallel$, $a_\perp$, ψ_i, and ϕ_i, with $i = 1, 2, 3$. These parameters are most likely to be obtained by calculating the flow field numerically, as they depend on exact object shapes. Nevertheless they are defined from steady-state flows with the object remaining fixed, thus avoiding the complicated moving boundary problems. Different numerical methods can be used for different cases. For example, the slender-body theory [17] is suitable if the object is composed of thin strings. For more general shapes, the boundary element method [4], by partitioning the object surface into small patches, can be used.

IV. ROTATIONAL DYNAMICS AND DRIFTING MOTION

First we consider the dynamics of $\hat{\boldsymbol{n}}$ (rotation), which is governed by

$$\begin{aligned} \frac{d\hat{\boldsymbol{n}}}{dt} &= \boldsymbol{\omega} \times \hat{\boldsymbol{n}} \\ &= \dot{\gamma} [\alpha_1 n_1 (\hat{\boldsymbol{n}} \times \hat{\boldsymbol{y}}) \times \hat{\boldsymbol{n}} + \alpha_2 n_2 (\hat{\boldsymbol{x}} \times \hat{\boldsymbol{n}}) \times \hat{\boldsymbol{n}}]. \quad (11) \end{aligned}$$

For nonchiral objects, $\psi_i = 0$; then $\alpha_1 = \phi_1/(\phi_1 + \phi_2)$ and $\alpha_2 = \phi_2/(\phi_1 + \phi_2)$. We recover the dynamics for a spheroid. With its orientation represented by a unit vector anchored at the origin, the tip could move on the surface of the unit sphere in the so-called closed Jeffery orbits [18]. There is a group of possible orbits under each ratio $\epsilon \equiv \phi_2/\phi_1$. Jeffery orbits for $\epsilon = 70$ (representative of a long object which has $\phi_2 \gg \phi_1$) are shown in Fig. 4(a), with equal-spaced orbits on the y–z plane.

Equation (11) shows that the chirality modifies the scalar orbit parameters, α_1 and α_2, but not the vector form. Thus the uniaxial chiral objects still rotate following the Jeffery orbits, with modified orbit parameters $\epsilon = \alpha_2/\alpha_1$.

Dynamical simulations [4] of straight twisted ribbons have found that the rotating motions did mostly follow the Jeffery orbits. Nevertheless the ribbons are seen to switch between different Jeffery orbits from time to time. Since the Jeffery orbits are closed curves, we believe that these switchings are likely due to thermal motions neglected in the analysis. One

FIG. 3. (a) Illustration for demonstrating $b_\parallel = 2\psi_3$. (b) For $b_\perp = \psi_1 + \psi_2$.
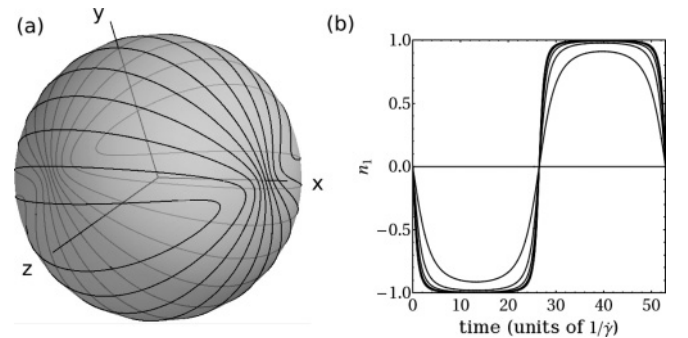
FIG. 4. (a) Jeffery orbits for $\epsilon = 70$, such as the case of a long object. (b) Time evolutions of n_1 components for the curves shown in (a). The one with the largest n_1 corresponds to the curve lying completely on the x–y plane in (a).

geometrical character in Fig. 4(a) is that the orbits cluster close to each other when $\hat{\boldsymbol{n}}$ orients close to the flow direction (x) but spread out from each other when on the velocity gradient-vorticity plane (y–z). Furthermore, the orientation spends a significant proportion of time staying near the flow direction, as shown in Fig. 4(b). Thus, near the flow direction, even small thermal motions could lead to switching of the Jeffery orbits.

Time evolutions of n_1, which is the component in the flow direction in Fig. 4(a), are shown in Fig. 4(b). The figure shows that a long object spends most of the time aligning near the flow direction. Since the drift motion will be shown later to depend on the time average of the helix orientation, for such cases, n_1 will have the dominant contribution, even with switching between different Jeffery orbits.

Next the drift/migration motions of the object in the vorticity (z) direction are obtained from Eq. (7) as

$$\boldsymbol{v} \cdot \hat{\boldsymbol{z}} = \dot{\gamma}\left(\beta_1 n_1^2 + \beta_2 n_2^2 - \beta_3 n_3^2\right) = \dot{\gamma}\beta\left(n_1^2 - n_2^2\right). \quad (12)$$

So the average migration speed of the chiral object is determined by the time average $\langle n_1^2 - n_2^2 \rangle$. Reverse of chirality could change signs of ψ_i and hence β. Two significant characters of Eq. (12) are that (1) there are no n_3 such that there will be no migration when $\hat{\boldsymbol{n}}$ aligns along the vorticity direction and (2) although migration speed depends on the orientation, there is only one migration coefficient β which is the same for all orientations.

If the object is a long helix, we have $\phi_1 \ll \phi_2$ (a larger torque when the helix aligns in the velocity-gradient direction, compared to in the flow direction). It is also expected that $q_\perp = a_\perp(\phi_1 + \phi_2) - (\psi_1 + \psi_2)^2 \approx a_\perp(\phi_1 + \phi_2)$ since the first term is the drag force and torque under shear for the overall rod shape, and the second term comes from the chiral property on top of the general shape. (This is indeed confirmed in our numerical calculations presented in the next section.) Then the migration coefficient β becomes

$$\beta \approx \psi_1 / a_\perp. \quad (13)$$

The obvious physical interpretation of Eq. (13) is that the coefficient is the force ψ_1 under shear divided by the drag coefficient. However, this migration coefficient also applies to all other helix orientations, even though ψ_1 is the force when the object is fixed and aligns in the flow direction. (Similar arguments also apply to a disk in which $\phi_2 \ll \phi_1$ and $\beta \approx -\psi_2 / a_\perp$.)

How does the helix still migrate with the coefficient $-\beta = -\psi_1 / a_\perp$ even when it is aligned in the y direction under a free rotation condition? For a long helix, $\alpha_1 \ll \alpha_2 \approx 1$, and at $\hat{\boldsymbol{n}} = \hat{\boldsymbol{y}}$ it will rotate with $\boldsymbol{\omega} = \dot{\gamma}\hat{\boldsymbol{z}}$. Thus the force balance equation (2), in the z direction is

$$-a_\perp v_z - b_\perp \dot{\gamma} + \psi_2 \dot{\gamma} = 0,$$

with $b_\perp = \psi_1 + \psi_2$, and we recover $v_z = -\dot{\gamma}\psi_1 / a_\perp$. This agrees with Eq. (12) at $n_1 = 0$ and $n_2 = 1$. On the other hand, when $\hat{\boldsymbol{n}} = \hat{\boldsymbol{x}}$, the rotation rate is very small, $\omega \approx 0$, and we have

$$-a_\perp v_z + \psi_1 \dot{\gamma} = 0,$$

giving $v_z = \dot{\gamma}\psi_1 / a_\perp$, again in agreement with Eq. (12).

V. NUMERICAL CALCULATIONS FOR LONG HELICES AND COMPARISONS WITH SIMULATION AND EXPERIMENT RESULTS

Thus we have derived the relevant chiral parameters for rigid body motion under shear, and particularly for the drift motion of a long helix we need only to evaluate two parameters, $a_\perp$ and ψ_1. Below, we will calculate them numerically using the boundary element method (see, e.g., Ref. [4]) for two geometries matching those used in previous simulations [4] and experiments [5]. Comparison of drifting velocities will be presented.

In Stokes flow, the flow field $\boldsymbol{v}(\boldsymbol{r})$ induced by the traction forces $\boldsymbol{f}(\boldsymbol{r})$ at a surface is given by the following, using the well-known Oseen tensor $H(\boldsymbol{r})$:

$$\boldsymbol{v}(\boldsymbol{r}) = \int_S H(\boldsymbol{r} - \boldsymbol{r}')\boldsymbol{f}(\boldsymbol{r}')dS(\boldsymbol{r}'). \quad (14)$$

We partition the object surface into small patches and assume the traction forces $\boldsymbol{f}_i$ to be constant over each patch i. Then, with the specification of fluid velocity $\boldsymbol{v}_i$ at each patch (matching the surface velocity due to the non-slip boundary condition), Eq. (14) leads to a system of linear algebraic equations determining the forces $\boldsymbol{f}_i$.

For the calculations of $a_\perp$, the helix is considered to move in the direction perpendicular to the center axis $\hat{\boldsymbol{n}}$. Thus $\boldsymbol{v}_i$ is a constant vector perpendicular to $\hat{\boldsymbol{n}}$. It is verified that if we consider a straight rod, with partition size approximately 0.2×0.2 with the rod radius being 1, our calculations give values of the drag coefficients $a_\perp$ and $a_\parallel$ within 3% of the known values.

For ψ_1, the situation corresponds to a fixed helix under external simple shear flow. Assume the simple shear flow $\boldsymbol{u}_s(\boldsymbol{r}) = -\dot{\gamma}y\hat{\boldsymbol{x}}$. We set the velocity on the helix surface to be $\boldsymbol{v}_i = -\boldsymbol{u}_s(\boldsymbol{r}_i)$ when solving Eq. (14). Thus the total flow field $\boldsymbol{u}_s(\boldsymbol{r}) + \boldsymbol{v}(\boldsymbol{r})$ will be zero at the object surface and match the simple shear at infinity.

First we compare our results with those obtained from dynamical simulations of chiral ribbons [4]. The simulations also included random motions whose strength is characterized by the Peclet number $P \equiv \dot{\gamma}/D_r$, with D_r being the rotational diffusion constant. Our result will correspond to the condition $P \gg 1$. For the geometry of the chiral ribbon used in Fig. 9 of Ref. [4], the drifting $\langle V_z \rangle / \dot{\gamma}a$ is 0.10, which agrees well with the value of 0.091 seen in the simulation results in Fig. 9 of Ref. [4] at $P \gg 1$. This agreement also confirms the validity of the uniaxial approximation for the long ribbons. It should be noted that the filled circles denoted as "our formula" in the said figure used the value for the chiral parameter g in Eq. (27) of Ref. [4] obtained from dynamical simulations. (Thus the comparison in the figure is mainly to show the correct dependence on P.)

We also consider the 25-turn helix with a geometry as the bacteria used experimentally in Ref. [5], with a string diameter of 143 nm, helix diameter 357 nm, and pitch length 643 nm. Even though uniaxial approximation was argued from a fast rotating average around the central axis compared to dynamics of orientation, we also check the variation of $\beta = \psi_1 / a_\perp$ with the helix at a different rotating angle with respect to the central axis. We find that the variations for both ψ_1 and $a_\perp$ are all

less than 1%. Thus even when the dynamical averaging is not complete we could still expect the uniaxial approximation to be valid.

For the discussions leading to the single chiral parameter β, we argued that the ratio $\phi_1/\phi_2 \ll 1$ and $(\psi_1 + \psi_2)^2 \ll |a_\perp(\phi_1 + \phi_2)|$ for long helices. Both conditions are indeed well satisfied with less than 1% errors.

The migration $\dot{\gamma}\beta$ is calculated to be 1.2 μm/s at the experimental shear rate $\dot{\gamma} = 103$ s^{-1}, with $\phi_2 \gg \phi_1$ here and $\hat{n}$ spending most of the time near the flow direction ($\hat{x}$) as in Fig. 4(b). The measured experimental value is 0.43 μm/s, which is about one-third of the calculated value. As noted in Ref. [5], this discrepancy is probably not too unreasonable considering that the helix still has some components in the vorticity direction (n_3) (e.g., due to diffusion) and other possible factors such as helix flexibility and interhelix hydrodynamic interaction.

Opposite to the long helix, consider the case of an object having a roughly spherical base shape with smaller chiral units grafted on the surface. One example is the chiral molecule composed of aromatic amide [15]. Choosing a particular axis through the center of the sphere as $\hat{n}$, the spherical base shape yields $a_\parallel \approx a_\perp$ (similarly for b and c), and $\psi_1 \approx \psi_2 \approx \psi_3$ (also for ϕ). Then we obtain $\beta \approx 0$. Thus we could expect a little drift motion for these kinds of objects in shear flows. Indeed it is also noted that, with the symmetry between n_1 and n_2

for a sphere, Eq. (12) requires a vanishing β for consistency. Similarly a chiral object with very strong rotational diffusion yielding a near isotropic distribution [4,5] would also have a vanishing β and migration.

VI. CONCLUSIONS

In conclusion, we solve the dynamical motions of uniaxial chiral objects under shear in low-Reynolds-number fluids. These solutions are parametrized in terms of object-flow interacting parameters in steady-state flow fields. Rotations are shown to follow the Jeffery orbits with the orbit parameters modified by the chirality, and drift/migration motions are determined by a unique chiral parameter. The physical origin of the single chiral parameter is explained, and good agreements with dynamical simulations are obtained. We believe that this analysis can be further extended to study other complex motions of chiral objects in nature situations and microfluidic cells, for example the dynamical interaction between chiral objects mediated by fluid flows.

ACKNOWLEDGMENTS

[1] Y. J. Kim and W. J. Rae, Int. J. Multiphase Flow **17**, 717 (1991).

[2] M. Kostur, M. Schindler, P. Talkner, and P. Hänggi, Phys. Rev. Lett. **96**, 014502 (2006).

[3] N. Watari and R. G. Larson, Phys. Rev. Lett. **102**, 246001 (2009).

[4] M. Makino and M. Doi, Phys. Fluids **17**, 103605 (2005).

[5] Marcos, H. C. Fu, T. R. Powers, and R. Stocker, Phys. Rev. Lett. **102**, 158103 (2009).

[6] J. Hill, O. Kalkanci, J. L. McMurry, and H. Koser, Phys. Rev. Lett. **98**, 068101 (2007).

[7] S. Sarman, Mol. Phys. **98**, 27 (2000).

[8] P. Chen and C.-H. Chao, Phys. Fluids **19**, 017108 (2007).

[9] S. Ahuja, *Chromatography and Separation Science* (Academic Press, New York, 2002); C. Fujimoto, Anal. Sci. **18**, 19 (2002); G. Gübitz and M. G. Schmid, Electrophoresis **23**, 3981 (2004).

[10] M. A. Osipov, B. T. Pickup, and D. A. Dunmer, Mol. Phys. **84**, 1193 (1995).

[11] T. C. Lubensky, A. B. Harris, R. D. Kamien, and G. Yan, Ferroelectrics **212**, 1 (1998).

[12] A. B. Harris, R. D. Kamien, and T. C. Lubensky, Rev. Mod. Phys. **71**, 1745 (1999).

[13] G. Bottari and T. Torres, Chem. Commun. **2004**, 2668 (2004).

[14] R. Herges, Chem. Rev. **106**, 4820 (2006).

[15] H. Masu, K. Katagiri, T. Koto, H. Kagechika, M. Tominaga, and I. Azumaya, J. Org. Chem. **73**, 5143 (2008).

[16] J. Happel and H. Brenner, *Low Reynolds Number Hydrodynamics with Special Applications to Particulate Media* (Prentice-Hall, Upper Saddle River, 1965).

[17] M. J. Kim and T. R. Powers, Phys. Rev. E **69**, 061910 (2004).

[18] G. B. Jeffery, Proc. R. Soc. A **102**, 161 (1922).